Trace Fe activates perovskite nickelate OER catalysts in alkaline media via redox-active surface Ni species formed during electrocatalysis

Liam Twight^a, Ally Tonsberg^a, Samji Samira^{b,c}, Kunal Velinkar^{c,d}, Kora Dumpert^a, Yingqing Ou^{a,e}, Le Wang^f, Eranda Nikolla^{c,d}, and Shannon W. Boettcher^{a,g*}

^a Department of Chemistry and Biochemistry and the Oregon Center for Electrochemistry, University of Oregon, Eugene, Oregon 97403, United States

^b Department of Chemical Engineering, University of California Santa Barbara, Santa Barbara, California, 93106, United States

^c Department of Chemical Engineering and Materials Science, Wayne State University, Detroit, Michigan 48202, United States

^d Department of Chemical Engineering, University of Michigan, Ann Arbor, Michigan 48109, United States

^e School of Chemistry and Chemical Engineering, Chongqing University, Chongqing 400044, China

^f Physical and Computational Sciences Directorate, Pacific Northwest National Laboratory, Richland, WA, 99354 United States

^g Department of Chemical & Biomolecular Engineering and Department of Chemistry, University of California, Berkeley, and Energy Storage and Distributed Resources Division, Lawrence Berkeley National Laboratory, Berkeley, CA 94720, United States

e-mail:

* Shannon W. Boettcher: <u>boettcher@berkeley.edu</u>

Abstract

The accurate description of activity trends among perovskite-oxide oxygen-evolution-reaction (OER) catalysts using electronic-structure descriptors requires that the bulk structure of the catalyst is comparable to that of the surface. Few studies have addressed the dynamic nature of the catalyst's structure during the OER and the consequential implications for understanding activity. Here, we use a combination of electrochemical and materials-characterization techniques to study the surface reconstruction and the associated formation of a new redox-active phase on LaNiO₃ particles, LaNiO₃ epitaxial films, and an analogous Ruddlesden-Popper phase, La₂NiO₄. Small, but characteristic, redox features corresponding to Ni redox in nominally amorphous NiO_xH_y are observed during cyclic voltammetry of these initially fully crystalline materials. The size of these redox features grows with prolonged cycling and contributes to an increased surface area as determined from electrochemical impedance spectroscopy (EIS). We find the OER activity is strongly dependent on soluble Fe species in the electrolyte, common impurities in alkaline media. These observations are consistent with the reconstruction of the crystalline surface to form NiO_xH_y species and subsequent activation by adsorption of Fe forming the well-known and extremely active NiFeO_xH_y OER catalyst.

Introduction

Perovskite oxides have been studied as oxygen evolution reaction (OER) electrocatalysts for decades due to their apparent high activity and use of relatively abundant transition metals [1]. Early efforts to rationalize the activity of these catalysts made use of activity correlations with bulk thermodynamic concepts such as lower-to-higher enthalpy of oxidation and d-electron count on the B-site metal cation [2]. More recently, descriptors such as the extent of transition-metal-oxygen hybridization (covalency) [3], O-2p band position band position relative to the Fermi energy [4], and e_g electron count of the transition metal cation [5] have been used to connect the activity of perovskite oxides to their electronic structures.

Bulk electronic structure descriptors can be useful for developing a physical and possibly predictive model for perovskite OER activity, as has been presented for the hydrogen-evolution reaction (HER) on metal surfaces [6-8]. However, the predictive power of these descriptors can be limited by dynamic processes that occur on the surface of perovskite oxides, causing large deviations of surface chemistry and composition from that of the bulk structure used to perform electronic-structure calculations [9]. In such a case, electronic descriptors might fail to accurately capture the relevant mechanistic parameters of the active surface. The most-dramatic and well-characterized examples of dynamic surface phenomena among perovskite oxides involve cobalt-based materials with partial substitution of alkaline-soluble species, like Sr²⁺,

at the A-site. Ba_{0.5}Sr_{0.5}Co_{0.8}Fe_{0.2}O₃(BSCF), was proposed to be active based on its optimal e_g electron count of around unity [5], but was later found to be unstable during OER [10]. Large proportions of the surface and eventually parts of the bulk "amorphized" via Sr-leaching and oxygen-vacancy formation forming an OER active Co(Fe)O_xH_y surface phase[10], similar to that made by other methods such as electrodeposition [11]. In a related study, a surface Co/Fe spinel oxide minority species on the underlying BSCF perovskite was determined to be responsible for dynamic, reversible conversion to an oxyhydroxide[12]. Sr-segregation and leaching, oxygen-vacancy formation, and subsequent surface reconstruction has also been clearly shown for the La_{1-x}Sr_xCoO₃ (LSCO) family of perovskites [13-15]. The implication of these studies is that rationalization of activity based on bulk electronics of the pristine BSCF and LSCO alone would fail to capture the real properties of the OER-active surface phase which has different oxidation states, composition, protonation state, and local structure. The active surface phase was, and likely is in many others, a completely different material. The intrinsic activity of the parent perovskite oxide with the pristine surface termination remains an open question. We hypothesize that, in fact, the presence of disordered conformationally dynamic surface phases with low activation barriers to rearrangement during the water-oxidation process is key to driving water oxidation at any reasonable overpotential.

The formation of nominally amorphous Co hydroxides has been observed on certain perovskites after OER and are active catalysts [16], especially in the presence of Fe impurities [17]. Whether formation of amorphous Ni hydroxides occur widely on nickelate perovskites is less clear. Inducing large structural changes by Sr-doping, as has been done with cobaltates, is not as accessible for nickelates because of the formation of impurities at low doping levels [18, 19]. Most of the insights so far have been from studies using epitaxial LaNiO₃ model systems[20]. Redox waves and thin ~2 unit cell-thick amorphous layers were observed by Bauemer et. al. and attributed to a NiO_xH_y-like species based on accompanying spectroelectrochemical data [21]. This work was recently extended, showing that redox-wave formation is also facet dependent with the highest stability and activity arising from the [111] facet. X-ray absorption fine structure analysis (XAFS) showed a new peak assigned to edge-sharing NiO₆ octahedra after 16 h chronoamperometry (2.5 V vs RHE), as had been observed for Sr-doped LaCoO₃ [22].

Localized amorphization on LaNiO₃ epitaxial films has been observed with TEM in a different study [23], but the role of these regions in OER was not discussed. Substitution of Sr^{2+} and Nd^{3+} at the Asite of such films improved the OER activity [24, 25], which was attributed to improvements in Ni-O hybridization from an upward shift in the O-2p band energy relative to the Fermi level and to optimal occupation of the B-site e_g antibonding orbital, respectively. Notably, the films with the best OER activity in these two studies also appear to have the largest redox-active Ni wave present in the cyclic voltammograms. Adiga and coworkers showed that Sr-leaching, Ni redox-wave formation, and surface amorphization occurs during cycling of La_{0.5}Sr_{0.5}Ni_{1-x}Fe_xO₃₋₈; evidence strongly suggestive of surface reconstruction[26]. Similar

redox waves were observed without Sr-doping in LaNi_{1-x}Fe_xO₃ (x = 0 - 0.5) with the largest being observed for x = 0.375 [27]. Bak *et al.* report a favorable "perturbation" (not amorphization) of oxygen octahedra in the near-surface layer of epitaxial perovskite nickelates after pre-reduction and pre-oxidation of the surface followed by exchange of Fe in the electrolyte. A related family of materials with high OER activity are the Ruddlesden-Popper oxides with formula (AO)(ABO_{3±δ})_n. Forslund and coworkers examined the family of compounds La_{0.5}Sr_{1.5}Ni_{1-x}Fe_xO_{4±δ} (x = 0-1) for trends in OER activity. They found that redox waves were present for all samples and the size, shape, and peak position differed as a function of Fe-content. Catalyst activity increased with Fe content up to x = 0.3 (interestingly near the solubility limit of Fe in NiO_xH_y) [28], then decreased as x increased to 1. This was attributed to Fe inducing a "cross-gap hybridization" that allowed optimal charge transfer through Fe-O-Ni bridges. Although surface amorphization was ruled out by pH-dependent measurements, no post-mortem TEM or other microscopy was reported [29].

If perovskite nickelates are reconstructing at the surface to the thermodynamically stable nickel (oxy)hydroxide, understanding the interaction of the surface with Fe impurities is imperative, yet is rarely explicitly probed. This is especially important to understand because NiO_xH_y is much more strongly activated by Fe than is CoO_xH_y [30]. Here we identify and analyze the emergence of redox-wave during/after OER catalysis on particulate and epitaxial LaNiO₃ samples and surface Ni-rich La₂NiO₄ nanorods which do not have any A-site or B-site doping. The size of the redox waves scale with the length of time of electrochemical treatment and their peak positions resemble that observed for NiO_xH_v. Upon introduction of Fe³⁺ into the Fe-free alkaline electrolyte, dramatic enhancement of the OER activity occurs along with an anodic peak shift of the redox waves for each sample. Normalization of the catalysts' OER currents to the integrated area of their redox waves suggests their activity in Fe-containing electrolyte is equivalent across the materials and in fact governed by the surface redox-active $Ni(Fe)O_xH_y$ or similar phases. Characterization with electrochemical impedance spectroscopy (EIS), atomic force microscopy (AFM), and Xray photoelectron spectroscopy (XPS) suggest surface reconstruction occurs on these materials, although direct imaging by transmission electron microscopy was unsuccessful; likely because the reconstructed layers are very thin and/or heterogeneously distributed. These insights are consistent with the formation of a Ni(Fe) O_xH_y -like surface phase. We argue that in any electrolyte not rigorously cleaned of Fe impurities, the intrinsic ability for a perovskite to generate surface redox-active Ni (as-determined from the integrated area of redox waves) should be considered as the primary descriptor for its OER activity.

Results and Discussion

Redox-active Ni is apparent from cycling and grows with cycle number. To investigate the structural stability of LaNiO₃ (LNO) and La₂NiO₄ (214-LNO) during OER, the catalysts were cycled between 50 - 100 times between 0 and 0.8 V vs. Hg|HgO (0.9 - 1.7 V vs RHE) in 1.0 M KOH at a scan rate

of 20 mV s⁻¹. Measurements were conducted in Fe-free and Ni-free 1 M KOH purified by methods detailed elsewhere [31, 32]. Catalyst films were made by spin-coating 80 μL of a 26.2 μg/μL ink which has a 5:1:1 mass ratio catalyst, acetylene carbon black, and Nafion (neutralized), respectively. Phase purity, powder morphology, and elemental composition of the LNO catalysts were confirmed by powder X-ray diffraction (PXRD), electron dispersive spectroscopy (EDX), scanning electron microscopy (SEM), and inductively coupled plasma mass spectroscopy (ICP-MS) given in Supplementary Figures 1, 2 and 3). The rod-shaped geometry and composition of 214-LNO as well as its tetragonal structure corresponding to the I4/*mmm* space group was confirmed using TEM imaging and X-ray diffraction (XRD) studies, respectively (Supplementary Figure 4 and 5). The Brunauer-Emmett-Teller surface areas were acquired from their nitrogen adsorption isotherms (Supplementary Figure 6). Epitaxial LNO was grown on LaAlO₃ substrates identically to those in Wang *et al.*[27], but without any aliovalent substitution. They were (001)-oriented and expected to have La-O termination based on the annealing temperature of 700°C used during synthesis [21], although the specific termination was not explicitly investigated in this study.

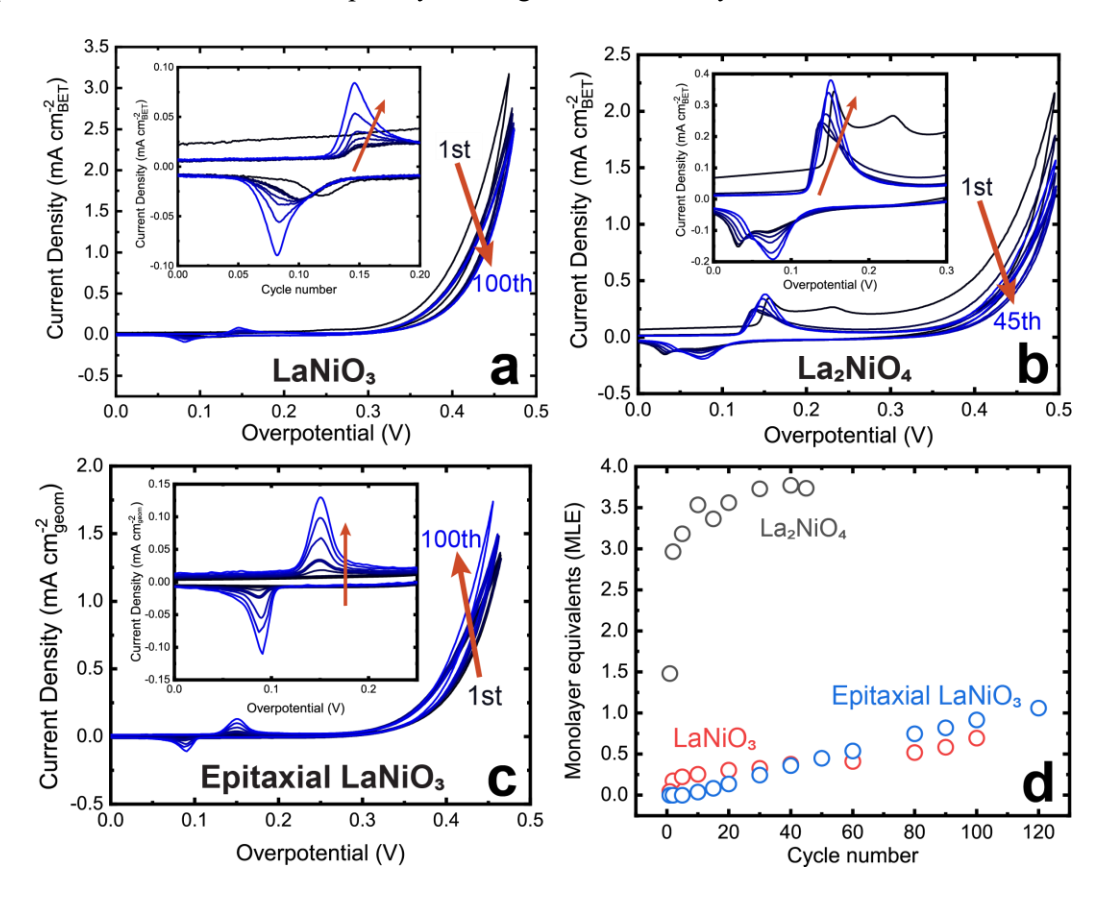


Figure 1. Extended cycling in Fe-free 1 M KOH of (a) particulate LNO (b) 214-LNO and (c) epitaxial LNO. Inset red arrows indicate the progression from first to last cycle. (d) the number of monolayer equivalents (MLE) of hydroxide calculated from the integrated charge of the peaks in (a-c) and BET surface area of the catalyst film.

We hypothesized that if LNO is thermodynamically unstable during OER, as has been posited as a

universal feature of oxides [33], restructuring to the stable NiO_xH_y phase would occur at the catalyst surface on a timescale dictated by the oxide material transformation kinetics. If the instability generated such a species, a minimum consequence would be observable Ni redox peaks. This follows from the observation that peak-like redox behaviour is not observed for a double-layer charging process where the electronic charge is in a band state and the ionic charge is in the double layer (unreconstructed nickelate), but it is observed when redox-active species are coupled to conducting surfaces and reside within the electrochemical double layer [34], as would be the case for surface phases of Co or Ni (oxy)hydroxide species formed from surface reconstruction. Such a structural change may also be evident in observable loss of crystalline phase purity, change in surface or bulk composition, and/or an increased nominal double-layer capacitance, depending on rate and extent. Figure 1 a-c shows the evolution of current response within the cyclic voltammograms of LNO, 214-LNO, and epitaxial LNO.

For all the nickelates shown in Figure 1, small but distinct pre-catalytic redox waves emerged and grew with continued cycling with comparable average peak positions of ~0.41 V vs Hg|HgO or 1.34 V vs RHE. There is also no clear plateau observed for this cycling protocol, suggesting further growth of the wave is possible. Future studies might investigate whether these waves plateau at a certain redox Ni coverage and/or amount of OER charge passed. The redox-peak positions agree with the known Ni²⁺/Ni³⁺ redox process of nominally amorphous nickel (oxy)hydroxides [35-37] but seem to be closer to those observed in ordered β-Ni(OH)₂ than in disordered α-Ni(OH)₂. This could stem from the influence of the crystalline LNO substrate on the *in-situ* grown Ni surface phase, leading to higher structural order. Such influence of the substrate structure on a grown overlayer is reminiscent of strain-induced electronic structure changes in epitaxial LaNiO₃ films [38]. The elemental composition of the films using ICP-MS are given in Supplementary Table 2, and in general did not change substantially from pristine stoichiometry after cycling.

For LNO, redox waves were initially small and could be easily missed in a study which was not explicitly looking for them. The epitaxial samples required ~ 20 cycles for the redox waves to become clearly observable. Baeumer *et al.* also observed distinct redox features in the pre-OER region when cycling single-crystal epitaxial LaNiO₃ films. The redox waves were immediately formed by the Ni-terminated films and their size decreased monotonically with increasing surface La termination. Redox-wave formation in that study was associated with the formation of amorphous 2 unit cell-thick NiO_xH_y [21]. That we see redox waves in this study shows that extended cycling may be crucial to reveal possible reconstruction when La termination is present. Using the geometric area of the epitaxial film, pseudo-cubic lattice parameters of 3.81 Å (from Wang *et al.*[27]), and the integrated charge from the 100th cycle we find that \sim 1.4 layers or 4.6% of the total Ni in the LNO epitaxial layer implicated in the redox. This increases to \sim 2 unit-

cell thickness (6% of the total Ni) after 145 cycles. Also notable is that the CVs of 214-LNO show two peaks during early cycles which merge into one in later cycles. This may occur by homogenization of two distinct redox Ni species by a dynamic surface process and cation mobility during cycling. Although we do not have direct evidence of this, the behavior resembles the process proposed to cause incorporation of "surface" Fe sites into the bulk/interior sites of NiO_xH_v [39].

These waves were confirmed not to be from Ni residues from the Fe-purification process. Ni amounts were routinely below the limit of ICP-MS detection of 0.57 ppb. Even if the maximum undetectable amount (~0.5 ppb) were present in a 10 mL volume electrolyte used in these experiments, the total amount of available Ni in the cell would only account for ~10% of the size of the largest redox waves. Further, we observe redox waves in Co(OH)₂-cleaned KOH (Supplementary Figure 7) and see no observable redox peaks when LaCoO₃ (Supplementary Figure 8) or a high-surface-area Pt coil (Supplementary Figure 9) is cycled. These control experiments show the source of the Ni redox waves as being the surface of the given catalyst. The OER activity also decreases over time in Fe-free conditions. Although this could be due to formation of a less-active surface species, in part this is also likely due to small O₂ bubbles that build-up on the surface of the electrode even under vigorous stirring, which we show in Supplementary Figure 10 likely decreases the active area by ~10%.

To understand if the redox-active changes in the Ni surface structure only stem from a cyclic application of voltage, we also performed chronoamperometric studies. It was found that redox-active Ni growth was not dependent on the cyclical application of voltage. Chronoamperometry (CA) at 0.8 V vs Hg/HgO of a spin-coated film of LNO was performed for 1 h with diagnostic CVs scanned at a rate of 20 mV s⁻¹ taken before the experiment and at 5-min intervals (Supplementary Figure 11). Integration of redox waves show that the amount of NiO_xH_y increases as a result of steady-state polarization. Immersion of a pristine electrode in 1.0 M KOH was performed to test if this increase could occur from electrolyte soaking alone. No change in the redox wave size occurred (Supplementary Figure 12). Application of anodic voltage was *required* for this Ni redox feature to increase in size.

If it is assumed the observed Ni-based redox features in Figure 1 originate from a (oxy)hydroxide-like structure, their integrated charge and catalyst BET surface area can be used to calculate a monolayer equivalent (MLE) of (oxy)hydroxide on the surface (Supplemental Calculation 1). This assumption is made based on the analogous behavior of the perovskite in the presence of Fe impurities to that of nickel (oxy)hydroxide and because we do not know the exact dimensions of the unit cells comprising the possibly reconstructed surface. The MLE value is the number of times the perovskite catalyst surface could be entirely covered by the redox-active Ni phase if it had the lattice parameters of β -Ni(OH)₂. Such an analysis would be particularly useful for characterizing these catalysts if it is confirmed that the redox species can be

modeled as NiO_xH_y formed by dissolution-redeposition of Ni cations and if this new phase dominates the OER activity. We note that after surface reconstruction it may be that either L a_z Ni_{1-z}O_xH_y, for example as directly accessed from mixed precursors, or separate LaO_xH_y and NiO_xH_y phases[40, 41], as reported from decomposition of La_{0.6}Sr_{0.4}CoO_{3- δ}, might be formed [42].

Using 1.7 nmol Ni cm⁻² for a single MLE based on the unit cell parameters for brucite β -Ni(OH)₂ (International Crystal Structure Database structure code: 169978), as discussed by Batchellor *et al.*[43], we find that the 214-LNO has 3.1 ± 0.5 MLE and LNO has 0.3 ± 0.1 MLE of nominally β -Ni(OH)₂ after 30 cycles. Because the MLE parameter is proportional to the amount of redox-active Ni per cm² on the surface, it captures the intrinsic ability of a given catalyst to produce these species. Figure 1d summarizes the evolution of this intrinsic capacity for redox with cycle number. Particulate LNO and epitaxial LNO show the same rate of MLE growth indicating they likely have similar surface chemistry. By contrast, 214-LNO rapidly formed ~ 3 MLE before the growth slows in later cycles. If the entire catalytic surface reconstructs homogeneously (that is, it does not form isolated pockets), and the surface species resembles NiO_xH_y, then given long duration electrolysis one could expect multiple monolayers of reconstructed surface on these nickelates.

The difference in observed intrinsic redox-active Ni can be explained by differences in surface termination and morphology between LNO and 214-LNO. Previous TEM and selected-area electron-diffraction (SAED) experiments show that the nanorods are primarily terminated by (001) facets along their longitudinal axis[44]. Previous work using depth-profiling low-energy ion-scattering spectroscopy (LEIS), atomic-resolution high-angle annular dark-field (HAADF) imaging, and electron energy loss spectroscopy (EELS) performed in aberration-corrected scanning TEM (STEM) mode revealed that these (001) facets were primarily Ni-O terminated rather than La-O terminated [45, 46]. By contrast we expect the epitaxial and LNO particulates to be primarily La-terminated because they were annealed at temperatures above that expected to promote Ni-termination [21]. Thus we attribute the difference in MLE quantity and initial restructuring rate to the pathways provided by the relatively Ni rich (001) surfaces of the nanorod bodies compared to LNO. The high proportion of Ni-terminated surface in the 214-LNO material could explain the faster rate of reconstruction of the first monolayer surface, but the apparent ease with which subsurface monolayers of NiO_xH_y form on 214-LNO suggest that the *sub* surface chemistry may also play a role. We hypothesize that oxygen non-stoichiometry and transport play roles in accessing the subsurface, especially considering that the electrochemical dissolution typically involves the formation of oxygen vacancies [13, 47] and oxygen is labile in the Ruddlesden-Popper oxides [48]. Further study is needed to understand how the concentration and formation energy of oxygen vacancies at the surface and bulk of these materials influences the restructuring process, if at all.

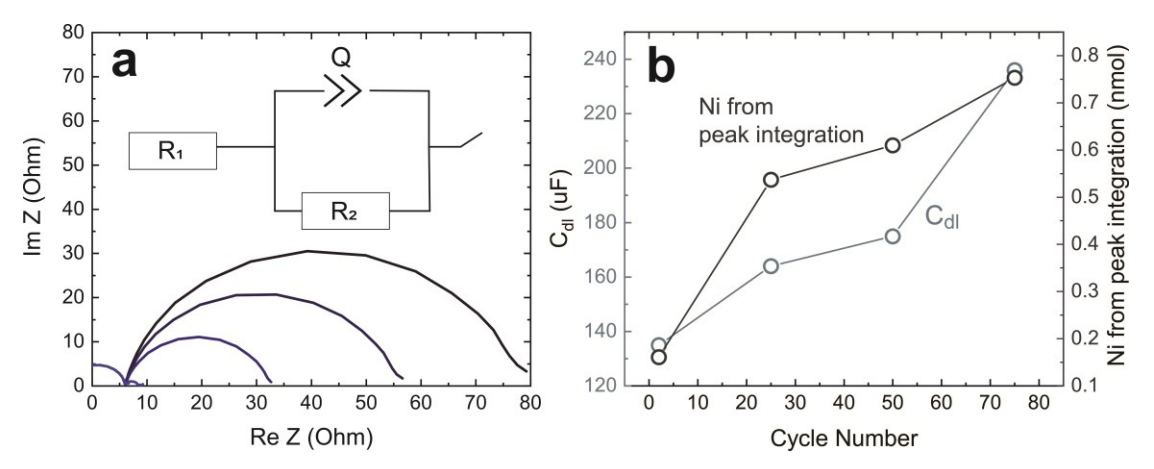


Figure 2. a) EIS of LNO at \sim 1.7 V vs RHE after 0, 25, 50, and 75 cycles in 1.0 M semiconductor grade KOH (not rigorously Fe-free) showing decreasing R_{CT} as a function of cycle number. The inset shows the equivalent circuit used to fit the data: solution and cell resistance, R_1 , in series with a Randles cell element with constant phase element Q parallel with faradaic impedance, R_2 . b) Double-layer capacitance (C_{dl}) and Ni from redox peak integrated area as a function of cycle number.

Surface reconstruction may also change the electrochemically active surface area. This can be probed from the double-layer capacitance ($C_{\rm dl}$) obtained via electrochemical impedance spectroscopy (EIS) [43]. Impedance scans were taken every 25 cycles up to 75 cycles of LNO in unpurified semiconductor grade KOH and are shown in Figure 2. Note that EIS was measured with the DC potential in the OER region (\sim 1.7 V vs RHE; 0.8 V vs Hg|HgO) rather than at open circuit because NiO_xH_y is only electronically conductive at potentials positive of the nominal Ni^{2+/3+} reduction potential [43]. The $C_{\rm dl}$ measured in the non-faradaic open-circuit potential region is representative only of the conductive support, not the active surface phase. The vertically compressed nature of the EIS semicircles led to us model the capacitive element as a constant phase element given in the inset of Figure 2a. Representative fit to the data is given in Supplementary Figure 13. The values of $C_{\rm dl}$ increased with prolonged cycling and the data directly mirror the increasing redox-active Ni from integrating the pre-OER redox wave. This result is consistent with the observed increase in surface area being due to the changing amount of Ni redox species at the LNO surface.

Assuming that the change in $C_{\rm dl}$ every 25 cycles is due to the formation of redox-active Ni phase, we can calculate the amount of Ni contributing to that change using the apparent capacitance per "monolayer equivalent" of NiOOH established from previous work [43]. Comparing this value to the change in redox-peak area, we find the two values are in good agreement (Supplementary Figure 14). Consistency between the amount of Ni from the redox wave and that predicted from EIS using NiOOH as a model [43] further suggests that the Ni redox from LNO can be assigned to a (oxy)hydroxide-like phase. The observed decreasing charge-transfer resistance is likely from the incorporation of trace Fe from semiconductor grade KOH in this experiment, which would also explain the slight improvement of activity during cycling compared to the slight decrease observed in the data in Figure 1. We note that Fe was not measured explicitly

here, and the role in activation by Fe impurities is discussed below.

LaNiO₃, La₂NiO₄, and epitaxial LaNiO₃ thin films are all activated by electrolyte Fe impurities.

After cycling, if the surface phase on LNO is nominally NiO_xH_v, the introduction of trace Fe impurities into rigorously Fe-free KOH electrolyte should increase OER activity via the formation of NiFeO_xH_y [49]. Following the extended cycling shown in Figure 1a-c, we spiked the electrolyte with 100 ppb Fe³⁺. As shown in Figures 3a-c, dramatic enhancement of the OER activity was observed for all samples. In general, the largest rate of activity increase per cycle is observed in the first 1-4 cycles after spiking, which slows to a near-constant rate after this primary activation event. The different rate of activity enhancement in earlier cycles compared to later ones can be explained by initial rapid Fe adsorption to redoxactive NiO_xH_v formed before the spike, making high-activity $Ni(Fe)O_xH_v$. In subsequent cycles, the current increases more slowly perhaps because all sites for Fe adsorption have been filled and formation of more high activity Fe sites is bottlenecked by the incremental increase in reconstructed Ni every cycle. Supplementary Figure 15 shows this constant incremental increase in later cycles in the full Fe spiked profile of an epitaxial LNO sample. Further, the magnitude of the enhancement observed in the first cycle immediately after Fe-spiking was variable, implying that the Fe-activation process is controlled by a mix of factors such as mass transport and accessibility of adsorption sites. Extended cycling (>100 CVs) is not necessary to observe an increase of activity after Fe spiking. Fe-based activity enhancement reproducibly occurs in as few as 8 cycles and with only 30 ppb of Fe³⁺ in the electrolyte, an amount below the solubility limit of Fe³⁺ in 1.0 M KOH [50] and comparable to that expected in high-purity commercial electrolytes that have not been rigorously cleaned of Fe [51] (Supplementary Figure 17). The latter observation aligns with activation from the uptake of soluble Fe and not from adsorption of FeOOH precipitate or colloids, although these may be relevant at higher Fe concentrations.

In a typical Fe-spiking experiment with electrodeposited NiO_xH_y, Fe adsorbs to nominally surface/edge sites immediately after spiking which increases the OER activity greatly, but the activity only marginally increases with further cycling and further Fe incorporation [49]. The Ni peak position also shifts anodically ~30 mV with 100 cycles in Fe-spiked conditions indicating strong interactions between Fe and the majority of the Ni sites [39, 49]. Using this result from Stevens *et al.*, we would expect an anodic shift of about 4 mV over 14 cycles (30 mV/100 cycles = 0.3 mV cycle⁻¹) if the redox-active Ni on LNO resembles NiO_xH_y. Interestingly, the peak position after spiking indeed shifts ~4 mV (inset of Figure 3a) in total. Rod-shaped La₂Ni₁O₄ nanostructures (214-LNO) and epitaxial LNO also exhibit the same general change in OER activity after Fe-spiking (inset of Figures 3b-c). Anodic shift of the redox peaks has been observed for La_{0.5}Sr_{1.5}Ni_{1-x}Fe_xO_{4+ δ} [29] increasing Fe substitution consistent with the growth of a NiFeOOH phase.

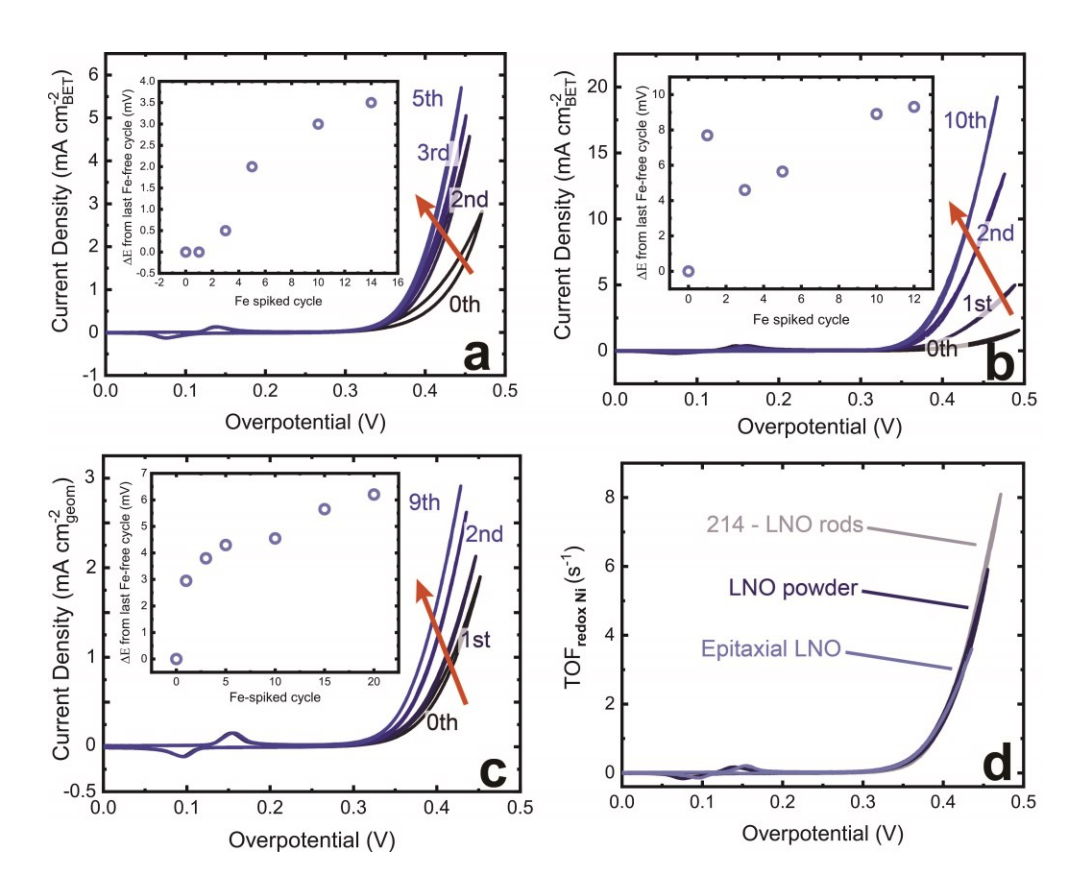


Figure 3. Comparison of activation of (a) particulate LaNiO₃, (b) La₂NiO₄ nanorods, and (c) epitaxial LaNiO₃ films upon introduction of 100 ppb Fe(NO₃)₃ into Fe-free 1.0 M KOH electrolyte at room temperature. The 0th cycle is the last Fe-free cycle before 100 ppb Fe was spiked into electrolyte. The insets illustrate the change in average redox peak position with cycle number. (d) TOF for the cycle corresponding to full activation by Fe (2nd or 3rd depending on the pace of activation) normalized to the redox active Ni from the integrated charge of the anodic redox peak of the 0th cycle. This data suggests that the active surface phases formed are the same on all three of the samples.

In the literature many electronic structure parameters have been suggested to describe such an activity difference between perovskites including position of the O-2p orbitals relative to the Fermi level [4] the filling of the antibonding e_g orbital [5, 52], and the charge-transfer energy Δ where smaller Δ is associated with increased Ni-O covalency [53]. We use the e_g orbital filling for La₂NiO₄ and LaNiO₃ as an example. This values has been calculated as ~0.74 and 0.91, for 214-LNO and LNO, respectively [54]. Based on the idea in many works that the best perovskite catalysts are those with near unity filling of e_g antibonding orbital of Ni [5] we would predict that LNO should outperform 214-LNO. In Fe-free conditions this appears to be case, but in Fe-spiked conditions (and therefore in realistic electrolysis conditions) this prediction fails (see the overlay of CVs after activation in Supplemental Figure 16).

Instead let us suppose the activity is dominated by a Ni(Fe) O_xH_y – like phase formed from the surface Ni and adsorbed Fe. We can then immediately rationalize the higher activity of 214-LNO because at any cycle, it will have a higher areal density of redox active Ni than LNO. It follows that if this NiFeO_xH_y

species has a similar intrinsic activity across the materials tested, then normalization of the current to the integrated Ni-related redox-peak area should yield equivalent polarization curves. This idea appears to be justified given the good match between samples once normalized to integrated charge (Figure 3d). Ultimately, these data illustrate that rather than a bulk electronic descriptor, a surface-chemical descriptor, namely, the surface density of redox-active Ni is a more suitable descriptor for activity under realistic conditions.

Because the introduction of Fe is a shared trait among these oxides, it can be used as a convenient indicator to determine whether the materials reconstruct, a strategy that has been highlighted recently in the $\text{Li}_x\text{Co}_{1-x}\text{O}_4$ family of materials [55]. Interestingly, we find that LaCoO_3 exhibits no such Fe activation (Supplementary Figure 8), which suggests its surface is more stable and does not as easily form cobalt-oxyhydroxide-like surface-phases generally consistent with previous literature [56]. Given that these materials are isostructural (rhombohedral, belonging to $R\bar{3}c$ space group) [57], we hypothesize that the enhanced stability with respect to surface-phase reconstruction arises from stronger Co-O bonding compared to Ni-O [58]. This is also consistent with the higher surface-reduction temperature as observed from H_2 temperature-programmed-reduction studies which indicate stronger Co-O bonding in $LaCoO_3$, as compared to Ni-O bonding in $LaNiO_3$ [57].

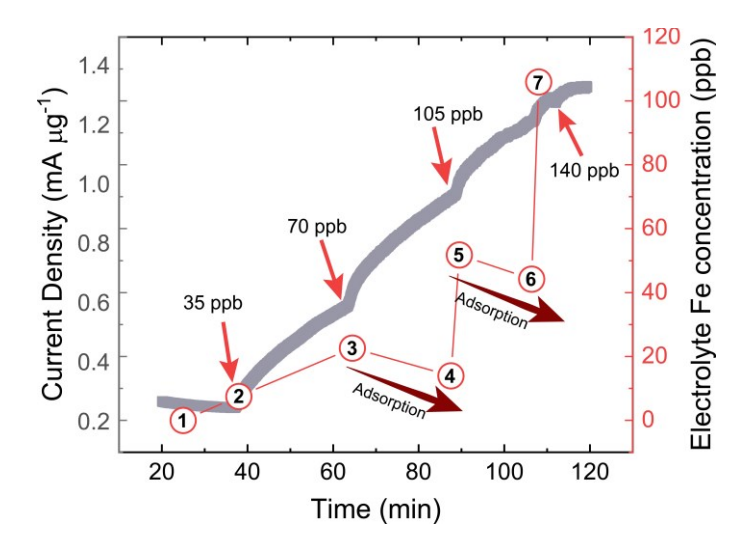


Figure 4. Chronoamperometry with intermittent Fe-spikes reported as mass activity versus time. Yellow arrows show points where a replicate additional Fe spike was performed. Concentration labels (black text) are the nominal Fe concentration at the time of the spike. Numbered circles indicate actual concentration of Fe (red axis) in the electrolyte measured from ICP-MS. This data shows Fe absorption from the electrolyte to the solid is coupled with increases in OER activity of the catalyst.

Activation of the reconstructed perovskites after spiking a small amount of Fe into 1.0 M KOH was evident in the cyclic voltammograms. Figure 4 shows 2 h of chronoamperometry at 1.7 V vs RHE on a

LNO electrode with additions of Fe at regular intervals. The yellow arrows indicate the approximate time and nominal concentration of electrolyte Fe after the spike while the red squares show the actual concentration of Fe in an aliquot of the electrolyte which was later measured by ICP-MS. The concentration of Fe in the electrolyte before the experiment was below the detection limit of ⁵⁷Fe in our ICP-MS of 3.9 ppb. Points 2, 3, 5, and 7 are aliquots of the electrolyte taken immediately after (~10 s) successive spikes of Fe. Points 4 and 6 are aliquots withdrawn before the corresponding spikes. Note that between the 2nd and 3rd, and 3rd and 4th spikes, the Fe concentration in the electrolyte decreases while the OER activity increases. This observation provides direct evidence that Fe adsorption from the electrolyte onto the electrode correlates with higher OER activity. Moreover, the impact of Fe adsorption on activity is noticeable even without performing any cyclic voltammetry, an observation which emphasizes that Tafel slopes and other activity parameters from chronoamperometric data must be collected in purified electrolyte for these materials to avoid strong effects of Fe-activation. Figure 4 also shows that pre-cycling the catalysts to generate redox active Ni is not necessary for increased activity in the presence of Fe; Fe enhancement should be expected from the moment the catalyst film adsorbs Fe.

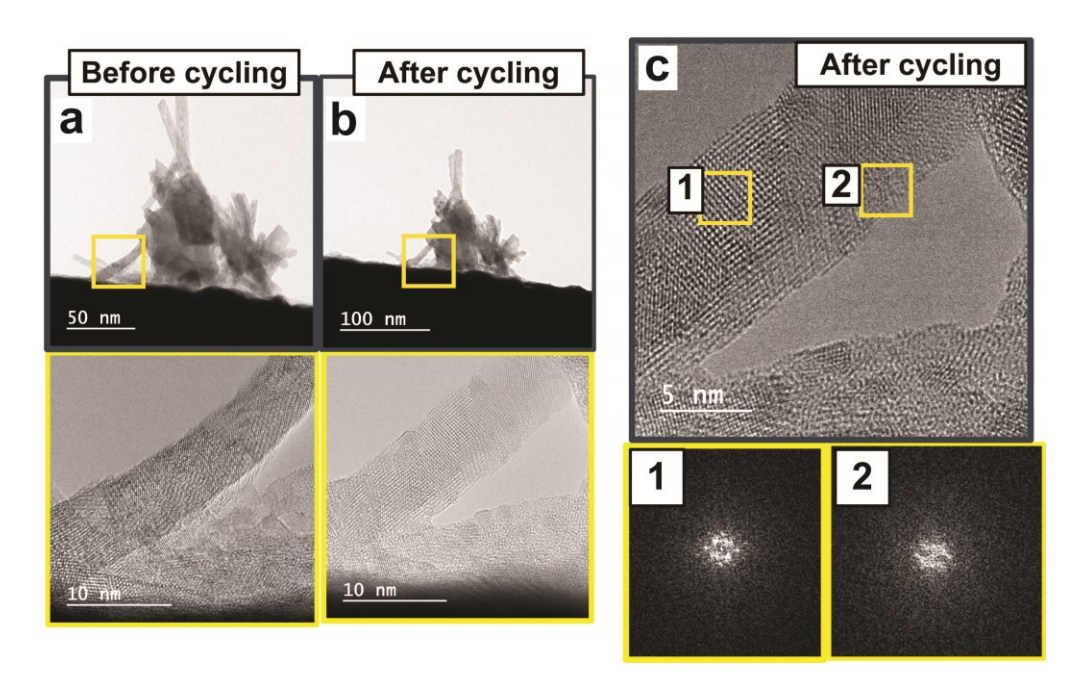


Figure 5. Identical-location TEM of a cluster of 214-LNO particles (a) before and (b) after 300 cycles on a gold TEM grid. Panel (c) shows fast Fourier transforms (FFTs) of two regions on the yellow boxed region. Comparing before and after cycling, the identical location appears to show a thicker nanorod. We suspect this is an artefact of non-identical imaging conditions and/or slit rotation of the nanorod during the electrochemical testing.

Identical location TEM (IL-TEM) was conducted on the LNO particulate materials before and after cycling with the aim of observing any obvious signs of structural changes such as amorphization. No clear

surface layers were observed, likely because of the near-atomic thinness of any reconstructed layers. The larger per-surface-area growth of redox-active Ni on 214-LNO would increase the likelihood of observing structural changes. Figures 5a-c show the near-surface structure of a cluster of 214-LNO nanorods before (Figure 5a) and after (Figure 5b-c) 300 cycles in 1.0 M KOH. The similar appearance of the cluster indicates that the same area and particles were successfully imaged both before and after cycling. We observed regions which apparently lack the crystalline order of neighboring areas after cycling as can be seen by the fast Fourier transform (FFT). This is a cautious interpretation because TEM studies can be subject to a variety of imaging artefacts, especially at edges, and over-interpretation. The disordered surface hydrated oxyhydroxide layers are thin, would be expected to scatter with low intensity, as they lack long range order, and may be unstable in the electron beam [59]. Selected-area electron-diffraction experiments did not suggest dramatic changes in crystal structure after cycling (Supplementary Figure 18 and Supplementary Table 1), consistent with the thinness of the surface-reconstructed layer. The inability to routinely observe reconstructed surfaces with TEM places a premium on careful electrochemical experiments as an alternative.

Finally, we performed post-mortem characterization by atomic force microscopy (AFM) and X-ray photoelectron spectroscopy (XPS) on the cycled, Fe-spiked epitaxial film corresponding to Figure 3c to learn about changes in the surface topology and chemical state. The 30-unit-cell films have a pseudocubic c-lattice parameter of ~3.81 Å [27] and are ~11 nm thick. The AFM scans shown in Figure 6 indicate roughening of the surface of the cycled film (arithmetic average roughness $R_a = 4.6$ nm) compared to the pristine film $R_a = 0.45$ nm consistent with previous AFM images of cycled epitaxial nickelate films [26, 27]. The magnitude of the roughness changes are highly suggestive of surface restructuring and formation of secondary phases which could be composed of one or more oxides or hydroxides of La, Ni and Fe. Assuming a component of the surface is NiO_xH_y, the large magnitude of the roughening could be driven by adsorbed Fe impurites by formation of Ni_zFe_{1-z}O_xH_y or FeO_xH_y in a manner observed when Fe is intentionally added to NiO_xH_y nanoplatelets [60, 61].

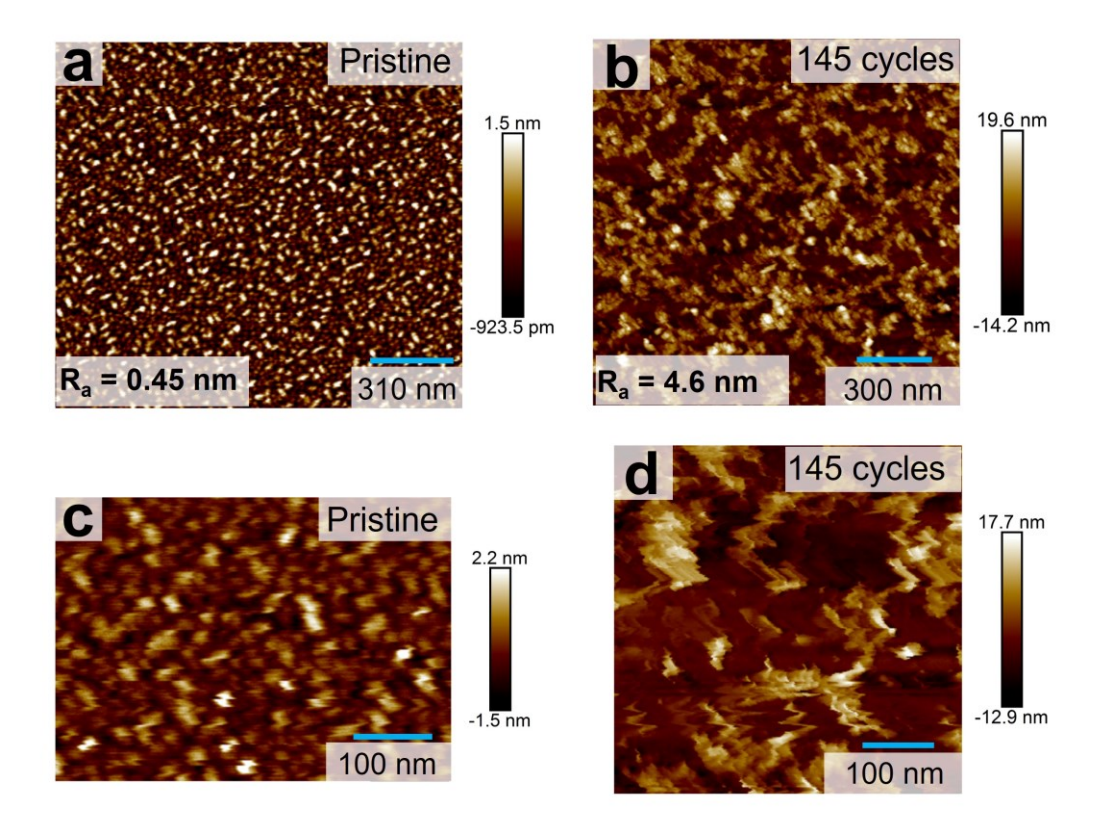


Figure 6. Atomic force microscopy image of that same (a,c) pristine epitaxial LNO film (note diffferent scales) and (b,d) the same film after cycled 120 times in Fe-free 1 M KOH followed by 25 times in 100 ppb Fe-spiked 1 M KOH. The arithmetic average roughness is given by R_a and indicates that cycling causes topological restructuring.

X-ray photoelectron spectroscopy (XPS) was used to detect the formation of new surface Ni phases on LNO electrodes after extended cycling (Figure 7). Unfortunately, the XPS spectra of the most intense lines – Ni 2p and La 3d – are difficult to interpret and deconvolute. Both Ni 2p and La 3d have multiplet structure and accompanying satellites [62-64], which directly interfere with each other. Consequently, little information was obtained from these regions. Therefore, we restrict our interpretation to the O 1s region where large, reproducible changes were observed. Figure 7 a, b shows the comparison of O 1s XPS for LNO and epitaxial LNO before and after extended cycling. After cycling, a significant decrease in the characteristic lattice oxygen feature located at ~528 eV was observed in the O 1s XPS core level spectra for both samples and resembles that of pure Ni(OH)₂ [65, 66]. Based on the cycling data in Figure 1, we estimated the depth of redox activity for the epitaxial sample would be about 1.5 nm after 300 cycles. Mild sputtering of the epitaxial film through the reconstructed surface with an argon cluster source caused the lattice oxygen peak to reemerge. The peak at higher binding energies, associated with weakly adsorbed oxygenated species and oxidized carbon, may also increase due to oxidation of the ionomer binder [67] and/or surface hydroxylation after exposure to alkaline electrolyte. Given the signs of reconstruction in the

cyclic voltammetry, EIS, and AFM, the loss of the lattice-oxygen feature is consistent with transformation to NiO_xH_y . The disappearance of the ~528 eV component within the O 1s spectra of initially crystalline nickel-based oxides upon electrochemical conditioning is not without precedent and has been shown to correspond to conversion of NiO to Ni(OH)₂ [36]. It has also been observed after cycling epitaxial LNO [26], similar to our observations.

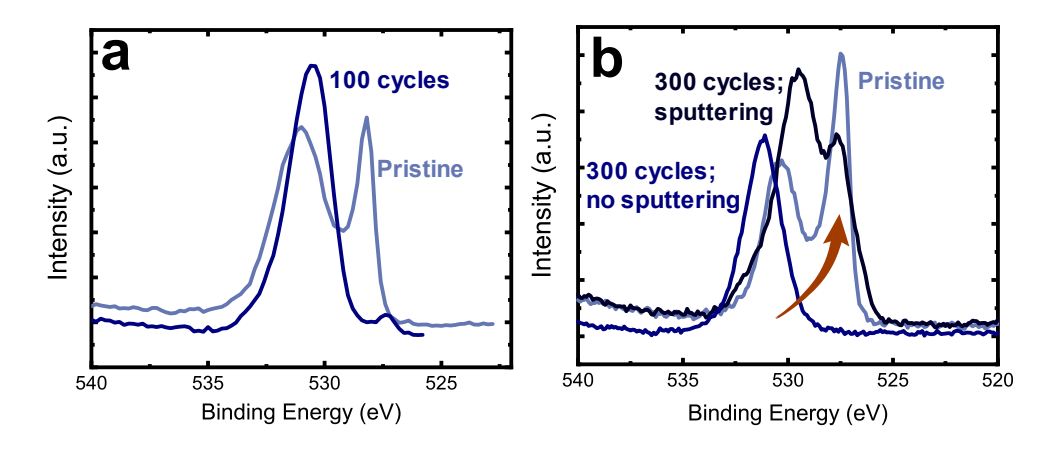


Figure 7. O 1s spectrum of **(a)** a spin-coated particulate LNO electrode before and after cycling and **(b)** an epitaxial LNO electrode after 300 cycles (dark blue), after mild sputtering with an argon ion source (black) and the pristine epitaxial sample (matte blue).

However, the decrease in intensity in the low binding-energy region might also arise from formation of a layer containing weakly adsorbed species like water, hydroxide, and/or adventitious carbon which could attenuate the signal originating from the underlying crystalline O²⁻. We tested whether the disappearance of the lattice oxide feature in epitaxial films occurs from immersion in KOH alone. Supplementary Figure 19 shows that the lattice oxygen feature is largely retained, implicating structural change from electrochemical treatment as the reason for the changes to the O 1s spectra. As shown in Figure 7, sputtering can be used to remove the layer of putative reconstructed material.

The broad role of restructuring in electrolysis. The results presented in this study adds a class of materials, perovskite and Ruddlesden-Popper oxide nickelates, to the growing roster of pre-catalysts where Fe impurities, whether introduced intentionally or not, play an important role in boosting OER activity. The role of Fe has already been well established among pure electrodeposited NiO_xH_y [35, 37, 68], Ni-based chalcogenides [69, 70], and CoO_xH_y [71]. A common theme emerging from these diverse materials is amorphization of A-site doped perovskite oxides, leading to the formation of active Fe-containing surface phases that are the actual agents responsible for catalysis [13, 72] and that these phases are the ones largely influenced by Fe impurities in the electrolyte. The interaction with Fe impurities holds critical implications not just for intrinsic activity studies of perovskite nickelates, *but for any investigation using electrocatalytic materials in alkaline electrolyzers*, which generally do not use highly purified electrolytes and

use stainless-steel components. The fact that nickelates with distinct structures, rhombohedral, oxygen-deficient particulate LaNiO₃, and tetragonal oxygen super-stoichiometric nanorod La₂NiO₄, are activated by Fe suggests these effects could be a universal phenomenon that has gone relatively unacknowledged. Interestingly, in this work the surface chemistry changes occurred in catalysts with full La-stoichiometry at the A-site while typically some substitution of the La at the A-site with an alkaline earth metal is required to observe instability in Co oxides[12, 13, 73, 74].

Other studies have also reported pH-dependent OER catalytic activity for perovskite oxides in which activity decreases with pH. This observation, coupled with isotopic oxygen labelling and on-line electrochemical mass spectroscopy data showing oxygen exchange, has led to the proposal of a lattice-oxygen-evolution (LOER) mechanism [23, 75]. An alternate proposal is that an oxidizing potential drives the reconstruction of the pristine material, a process which requires oxygen lability and exchange. The new surface species may be sensitive to soluble Fe, especially when the B-site is occupied by Ni or Co. Consequently, the decreasing activity with decreasing pH could be, at least in part, due to the corresponding decrease in soluble Fe by an order of magnitude with each unit decrease in pH, as has been suggested recently for La_{1-x}Sr_xCoO₃ [13]. Since lattice-oxygen exchange has been detected for NiO_xH_y [76], it is still not clear whether LOER after reconstruction is from the perovskite or the *in-situ* formed NiO_xH_y.

Conclusions

Both LaNiO₃ and La₂NiO₄ exhibit a growth of redox-active Ni species that increases in quantity as a function of cycling and duration of chronoamperometric conditioning. Fe-spiking experiments demonstrate that high OER activity is achieved upon the introduction of Fe. After Fe introduction, further activity increase with cycle number correlates with the increased quantity of redox-active Ni. Analysis of impedance spectroscopy, XPS and TEM data support the proposal here that generation of redox-active surface species involves a structural transformation leading to increased electrochemically active surface area with cycling, a decrease in nominally surface O2- content compared to -OH, and the nominal amorphization of the catalyst. Normalization of the catalytic current to the integrated charge corresponding to redox-active Ni available during the Fe spike experiments show that the redox-active species share similar OER activity characteristics despite disparate structures of the host LaNiO₃ and La₂NiO₄. La₂NiO₄ displays a higher tendency for the growth of redox-active Ni than LaNiO₃, indicating the significance of Ni-O termination in the formation of these surface species. Although the analogy between the reconstructed perovskite surface in Fe-spiked conditions and NiFeO_x H_{ν} is strong, the precise surface structure remain under debate and the characterization here is not sufficiently detailed to settle it. Surface-sensitive X-ray absorption fine stucture analysis and in situ XRD studies would be extremely valuable for reconciling the electrochemical observations here to the bulk structure of the perovskites.

The data and analyses reported here show that interpretations of intrinsic activity and the correlation of this activity to electronic and structural features of the pristine material necessitate Fe-free conditions and pre- and post-mortem surface analysis. Reports of intrinsic activity of nickelate perovskites and related materials should be made with caution - especially if only a single voltammetry sweep or chronoamperometry is performed in unpurified electrolytes without paying close attention to pre-catalytic redox waves which may become prominent with further cycling. The implications of these results are that in any practical alkaline electrolyzer system (unpurified 30 wt% KOH and with stainless-steel cell components) the activity of a perovskite nickelate catalyst will be controlled by its extent of surface reconstruction and interactions with Fe impurities. Future effort could focus on characterizing and tailoring the catalyst composition, along with the precise electrolye composition, to tune the activity and stability of this surface phase. The formation of these surface phases, their interaction with the underlying substrate, and catalytic turnover of intermediates, must fundamentally be related to nature of bonding within the material as well as adsorbates, and therefore its electronic structure. The use of descriptors from quantum-mechanical calculations of electronic structure to understand structure-restructuring relationships in the presence of potential, water, and alkali electrolyte would thus be a valuable addition to the field of heterogeneous OER electrocatalysis. Such approaches would complement typical calculations of intermediate binding energies [77].

Methods and Materials

Synthesis. LaNiO₃ was prepared using a nitrate precipitation method. 1.95 mmol of nickel (II) nitrate hexahydrate and 2 mmol lanthanum (III) nitrate nonahydrate was weighed out and dissolved in 10 mL 18.2 M Ω nanopure water. A slight under-stoichiometry was chosen for the nickel nitrate to prevent minor NiO species formation. A mixed La/Ni hydroxide was precipitated by rapid addition of a 4 mL + 4 mL mixture of water and semiconductor-grade tetramethylammonium hydroxide. The resulting mixture was stirred for 30 min to ensure complete reaction. The solid was recovered with centrifugation, ground in an agate mortar and pestle for 5 min and calcined in air at 900 °C for 12 h. The solid was ground and refired until phase-pure samples were obtained based on powder X-ray diffraction (PXRD) patterns. La₂NiO₄ rods were prepared using a reverse microemulsion procedure described in prior work [44]. A reverse-microemulsion-based technique was used for the synthesis of rod-shaped La₂NiO₄ (214-LNO) nanostructures [45, 78]. A typical synthesis of 214-LNO involved the reaction between two quaternary phase microemulsions. Both the microemulsions contained equal amounts of cetyltrimethylammonium bromide (CTAB; 11.0 g), hexane (Sigma Aldrich, HPLC grade), and n-butanol (Sigma Aldrich >99%). The difference between the two microemulsions was that one of the microemulsions contained stoichiometric amounts of La(NO₃)₃·6H₂O (Sigma Aldrich, >99.999%) and Ni(NO₃)₂·6H₂O (Sigma Aldrich, >98%) salts (2 mmol equivalent) dissolved in 1.155 mL of deionized (DI) water (>18.2 MΩ). KOH solution was used in the anionic microemulsion to aid in precipitation of the hydroxides. The morphology of the samples can be

changed by varying the ratio of water used to dissolve salts and that of CTAB. A water to CTAB ratio of 1.6 was used to obtain rod-shaped 214-LNO nanostructures. The two microemulsions were mixed and subsequently allowed to react for 4 h to form a sol-gel mixture of metal hydroxides. Subsequently, the formed hydroxides were collected by centrifugation, and washed three times with ethanol and three times with deionized water. The precipitate was dried in an oven in air at 80 °C overnight, followed by calcination in Ar at 835 °C for 2 h (heating rate: 2 °C/min).

Epidtaxial LaNiO₃ thin films with the thickness of 20 unit cells (~8 nm) were grown on (001) oriented LaAlO₃ substrates by using O₂-plasma–assisted molecular beam epitaxy (OPA-MBE). The growth details have been described elsewhere and films prepared in this manner are expected to yield a surface with a (001) orientation [25]. The substrate temperature was set to 700 °C during growth which is expected to yield primarily La-O termination based on the report by Baeumer, *et al.*[21] although this was not explicitly investigated here.

Electrochemical measurements. Catalyst films were either prepared by spin-coating or by dropcasting onto Pt/Ti-coated (25 nm Pt on 50 nm Ti) glass slides made using electron beam evaporation. Choice of coating technique is indicated for the given data in the text. Spin-coated films were chosen for intrinsic activity measurements so that electron-transport distances were reduced relative to drop-cast films and conductive binder, which oxidizes during OER, could be excluded in ink preparation. Ink for spin-coating was ~5:1 by mass of catalyst to Nafion binder suspended in solvent of 2:1 by volume of isopropanol to nanopure water. Inks were sonicated for at least 1 h before coating. A typical spin-coating procedure involved adding ~80 uL onto the substrate after sonication and spinning at 3000 RPM for 2 min. Nafion was neutralized with a few drops of Fe-free 1.0 M KOH to avoid possible dissolution of the catalyst by reaction with acidic groups. Spin-coated Ti/Pt slide pieces were then assembled into working electrodes as described elsewhere [79]. All electrochemical measurements were performed in Fe/Ni free 1.0 M KOH (prepared from semiconductor-grade KOH using the standard methods from our team [32]) using a Hg[HgO reference electrode calibrated against RHE and Pt coil counter electrode. Plastic cells were used and cleaned with 1.0 M sulfuric acid before experimentation to remove trace Fe from the cell. All electrochemistry was performed using a Biologic SP-300 potentiostat. Impedance spectroscopy was performed from 1 Hz to 7 MHz from the DC voltage of 0.8 V vs Hg|HgO with 10 mV AC amplitude. The impedance data was fit to the equivalent circuit depicted as an inset in Figure 3b; the circuit includes a solution and cell resistance, R1, in series with a Randles cell element with constant phase element Q2 parallel with faradaic impedance, R2. A constant phase element was chosen because its impedance is similar to that of a pure capacitance, but more closely fit the slightly depressed semicircular shape of the measured impedance. Uncompensated series resistance (R_u) was extracted using impedance spectroscopy at 0 V vs Hg|HgO from 1 Hz to 1 MHz and was estimated from the associated Nyquist plot as the value of the real component of the impedance at high frequencies

where the imaginary impedance approaches zero. All electrochemical data is iR_u -corrected unless otherwise indicated.

Characterization. XRD studies were performed using a powder diffractometer (Bruker D2 Phaser) with a Cu Kα source. Scans were obtained between a 2θ of 20-80°. ICP-MS measurements (ThermoFisher iCAP-RQ) were performed in kinetic energy discrimination mode with calibrations of all measured elements having R² values > 0.998. All digestions of catalyst films were done with concentrated TraceMetal® grade nitric acid (Fisher Scientific). Laboratory control standards containing known amounts of La, Ni, Fe, and Co were run at intervals between unknown samples to continually verify good performance of hardware and internal standards. XPS studies were done using an ESCALAB 250 (ThermoScientific). Spectra were obtained using an Al Kα monochromated (150 W, 20 eV pass energy, 500μm spot size) X-ray source. All samples were optimally charge-neutralized using an in-lens electron source combined with a low-energy Ar⁺ flood source. TEM data was acquired using a FEI 80-300 kV (S)TEM equipped with a spherical aberration image corrector. All data was collected at 300 kV. For IL-TEM experiments, a PELCO gold pinpointer grid (400 mesh, Ted Pella) was dip-coated by repeated rounds of immersion into the catalyst ink until a visible change of the grid color to that of the ink was achieved. Loading was not measured or controlled since only some locations with good contact between grid and catalyst were required for these studies. Powder X-ray diffractograms were obtained with a benchtop Bruker D2 Phaser.

For BET surface area experiments, 50-80 mg of samples were loaded into BET sample tubes without the use of solvent, ensuring that sample did not touch the neck of the BET tube. Then, samples were degassed under high vacuum at 170 °C on a Micromeritics ASAP 2020. Degassing was considered complete when the outgas rate fell below 2.5 μ torr/min. Once the degassing was completed, the samples were subjected to N_2 surface sorption measurements and BET surface area was calculated.

Acknowledgements

This work was supported by the National Science Foundation Chemical Catalysis Program, Award # 1955106. The ICP-MS instrument was funded by an NSF MRI Award #2117614. E.N. acknowledges the financial support from the United States Department of Energy (DOE), Basic Energy Science (BES), Chemical Sciences, Geosciences, and Biosciences Division, under award number DE-SC0020953/DE-SC0023645. Synthesis of LaNiO₃ epitaxial thin films was supported by the U.S. Department of Energy (DOE), Office of Science, Basic Energy Sciences, Division of Materials Sciences and Engineering, Synthesis and Processing Science Program, under Award #10122. We gratefully acknowledge Josh Razink for support with TEM measurements, support from Steve Golledge with XPS spectra acquisition, and Aaron Kaufman for AFM measurements.

Author contributions

L.T. and S.B. conceived of the research with assistance from Y.O. S.W.B. directed the research project. L.T. collected most of the experimental data, with assistance from A.T. and K.D.; K.V. and S.S. directed by E.N. synthesized and characterized the R-P 214-LNO materials as well as advised on their properties. L. W. prepared the epitaxial LaNiO₃ films. L.T and S.W.B. analyzed the data and L.T. wrote the manuscript with contributions from S.B., E.N., K.V, S.S, and L.W.

Data availability

The data supporting the findings of this study are available from the authors upon request.

References

- [1] E. Fabbri, T.J. Schmidt, Oxygen Evolution Reaction—The Enigma in Water Electrolysis, ACS Catal., 8 (2018) 9765-9774, https://doi.org/10.1021/acscatal.8b02712
- [2] J.O.M. Bockris, T. Otagawa, Mechanism of oxygen evolution on perovskites, J. Phys. Chem., 87 (1983) 2960-2971, https://doi.org/10.1021/j100238a048
- [3] J. Song, X. Jin, S. Zhang, X. Jiang, J. Yang, Z. Li, J. Zhou, H. Zhang, Y. Nie, Synergistic Role of Eg Filling and Anion—Cation Hybridization in Enhancing the Oxygen Evolution Reaction Activity in Nickelates, ACS Appl. Energy Mater., 4 (2021) 12535-12542, https://doi.org/10.1021/acsaem.1c02335
- [4] L. Giordano, K. Akkiraju, R. Jacobs, D. Vivona, D. Morgan, Y. Shao-Horn, Electronic Structure-Based Descriptors for Oxide Properties and Functions, Acc. Chem. Res., 55 (2022) 298-308, https://doi.org/10.1021/acs.accounts.1c00509
- [5] J. Suntivich, K.J. May, H.A. Gasteiger, J.B. Goodenough, Y. Shao-Horn, A perovskite oxide optimized for oxygen evolution catalysis from molecular orbital principles, 334 (2011) 1383-1385, https://science.sciencemag.org/content/334/6061/1383.long
- [6] B. Hammer, J.K. Nørskov, Electronic factors determining the reactivity of metal surfaces, Surf. Sci., 343 (1995) 211-220, https://www.sciencedirect.com/science/article/pii/0039602896800070
- [7] B. Hammer, J.K. Norskov, Why gold is the noblest of all the metals, Nature, 376 (1995) 238-240, https://doi.org/10.1038/376238a0
- [8] B. Hammer, J.K. Nørskov, Theoretical surface science and catalysis—calculations and concepts, in: Adv. Catal., Academic Press, 2000, pp. 71-129.
- [9] F. Calle-Vallejo, O.A. Díaz-Morales, M.J. Kolb, M.T.M. Koper, Why Is Bulk Thermochemistry a Good Descriptor for the Electrocatalytic Activity of Transition Metal Oxides?, ACS Catal., 5 (2015) 869-873, https://doi.org/10.1021/cs5016657
- [10] E. Fabbri, M. Nachtegaal, T. Binninger, X. Cheng, B.-J. Kim, J. Durst, F. Bozza, T. Graule, R. Schäublin, L. Wiles, M. Pertoso, N. Danilovic, K.E. Ayers, T.J. Schmidt, Dynamic surface self-reconstruction is the key of highly active perovskite nano-electrocatalysts for water splitting, Nat. Mater., 16 (2017) 925-931, https://doi.org/10.1038/nmat4938
- [11] M.S. Burke, M.G. Kast, L. Trotochaud, A.M. Smith, S.W. Boettcher, Cobalt–Iron (Oxy)hydroxide Oxygen Evolution Electrocatalysts: The Role of Structure and Composition on Activity, Stability, and Mechanism, J. Am. Chem. Soc., 137 (2015) 3638-3648, https://doi.org/10.1021/jacs.5b00281

- [12] T.-H. Shen, L. Spillane, J. Vavra, T.H.M. Pham, J. Peng, Y. Shao-Horn, V. Tileli, Oxygen Evolution Reaction in Ba_{0.5}Sr_{0.5}Co_{0.8}Fe_{0.2}O_{3-δ} Aided by Intrinsic Co/Fe Spinel-Like Surface, J. Am. Chem. Soc., 142 (2020) 15876-15883, https://doi.org/10.1021/jacs.0c06268
- [13] P.P. Lopes, D.Y. Chung, X. Rui, H. Zheng, H. He, P. Farinazzo Bergamo Dias Martins, D. Strmcnik, V.R. Stamenkovic, P. Zapol, J.F. Mitchell, R.F. Klie, N.M. Markovic, Dynamically Stable Active Sites from Surface Evolution of Perovskite Materials during the Oxygen Evolution Reaction, J. Am. Chem. Soc., 143 (2021) 2741-2750, https://doi.org/10.1021/jacs.0c08959
- [14] A. Boucly, L. Artiglia, E. Fabbri, D. Palagin, D. Aegerter, D. Pergolesi, Z. Novotny, N. Comini, J.T. Diulus, T. Huthwelker, M. Ammann, T.J. Schmidt, Direct evidence of cobalt oxyhydroxide formation on a La_{0.2}Sr_{0.8}CoO₃ perovskite water splitting catalyst, J. Mater. Chem. A, 10 (2022) 2434-2444, http://dx.doi.org/10.1039/D1TA04957G
- [15] A. Boucly, E. Fabbri, L. Artiglia, X. Cheng, D. Pergolesi, M. Ammann, T.J. Schmidt, Surface Segregation Acts as Surface Engineering for the Oxygen Evolution Reaction on Perovskite Oxides in Alkaline Media, Chem. Mater., 32 (2020) 5256-5263, https://doi.org/10.1021/acs.chemmater.0c01396 [16] T. Wiegmann, I. Pacheco, F. Reikowski, J. Stettner, C. Qiu, M. Bouvier, M. Bertram, F. Faisal, O. Brummel, J. Libuda, J. Drnec, P. Allongue, F. Maroun, O.M. Magnussen, Operando Identification of the Reversible Skin Layer on Co₃O₄ as a Three-Dimensional Reaction Zone for Oxygen Evolution, ACS
- [17] T. Zhang, M.R. Nellist, L.J. Enman, J. Xiang, S.W. Boettcher, Modes of Fe Incorporation in Co–Fe (Oxy)hydroxide Oxygen Evolution Electrocatalysts, ChemSusChem, 12 (2019) 2015-2021, https://doi.org/10.1002/cssc.201801975
- [18] F.S. Oliveira, P.M. Pimentel, R.M.P.B. Oliveira, D.M.A. Melo, M.A.F. Melo, Effect of lanthanum replacement by strontium in lanthanum nickelate crystals synthetized using gelatin as organic precursor, Mater. Lett., 64 (2010) 2700-2703,
- https://www.sciencedirect.com/science/article/pii/S0167577X10007093

Catal., 12 (2022) 3256-3268, https://doi.org/10.1021/acscatal.1c05169

- [19] R. Sankannavar, K.C. Sandeep, S. Kamath, A.K. Suresh, A. Sarkar, Impact of Strontium-Substitution on Oxygen Evolution Reaction of Lanthanum Nickelates in Alkaline Solution, J. Electrochem. Soc., 165 (2018) J3236, https://dx.doi.org/10.1149/2.0301815jes
- [20] Y. Sun, C.-R. Wu, T.-Y. Ding, J. Gu, J.-W. Yan, J. Cheng, K.H.L. Zhang, Direct observation of the dynamic reconstructed active phase of perovskite LaNiO₃ for the oxygen-evolution reaction, Chem. Sci., 14 (2023) 5906-5911, http://dx.doi.org/10.1039/D2SC07034K
- [21] C. Baeumer, J. Li, Q. Lu, A.Y.-L. Liang, L. Jin, H.P. Martins, T. Duchoň, M. Glöß, S.M. Gericke, M.A. Wohlgemuth, M. Giesen, E.E. Penn, R. Dittmann, F. Gunkel, R. Waser, M. Bajdich, S. Nemšák, J.T. Mefford, W.C. Chueh, Tuning electrochemically driven surface transformation in atomically flat LaNiO₃ thin films for enhanced water electrolysis, Nat. Mater., 20 (2021) 674-682, https://doi.org/10.1038/s41563-020-00877-1
- [22] A. Füngerlings, M. Wohlgemuth, D. Antipin, E. van der Minne, E.M. Kiens, J. Villalobos, M. Risch, F. Gunkel, R. Pentcheva, C. Baeumer, Crystal-facet-dependent surface transformation dictates the oxygen evolution reaction activity in lanthanum nickelate, Nat. Commun., 14 (2023) 8284, https://doi.org/10.1038/s41467-023-43901-z
- [23] J. Liu, E. Jia, K.A. Stoerzinger, L. Wang, Y. Wang, Z. Yang, D. Shen, M.H. Engelhard, M.E. Bowden, Z. Zhu, S.A. Chambers, Y. Du, Dynamic Lattice Oxygen Participation on Perovskite LaNiO₃ during Oxygen Evolution Reaction, J. Phys. Chem. C, 124 (2020) 15386-15390, https://doi.org/10.1021/acs.jpcc.0c04808
- [24] L. Wang, K.A. Stoerzinger, L. Chang, J. Zhao, Y. Li, C.S. Tang, X. Yin, M.E. Bowden, Z. Yang, H. Guo, L. You, R. Guo, J. Wang, K. Ibrahim, J. Chen, A. Rusydi, J. Wang, S.A. Chambers, Y. Du, Tuning Bifunctional Oxygen Electrocatalysts by Changing the A-Site Rare-Earth Element in Perovskite Nickelates, Adv. Funct. Mater., 28 (2018) 1803712, https://doi.org/10.1002/adfm.201803712 [25] J. Liu, E. Jia, L. Wang, K.A. Stoerzinger, H. Zhou, C.S. Tang, X. Yin, X. He, E. Bousquet, M.E.
- Bowden, A.T.S. Wee, S.A. Chambers, Y. Du, Tuning the Electronic Structure of LaNiO₃ through

- Alloying with Strontium to Enhance Oxygen Evolution Activity, Advanced Science, 6 (2019) 1901073, https://doi.org/10.1002/advs.201901073
- [26] P. Adiga, L. Wang, C. Wong, B.E. Matthews, M.E. Bowden, S.R. Spurgeon, G.E. Sterbinsky, M. Blum, M.-J. Choi, J. Tao, T.C. Kaspar, S.A. Chambers, K.A. Stoerzinger, Y. Du, Correlation between oxygen evolution reaction activity and surface compositional evolution in epitaxial $La_{0.5}Sr_{0.5}Ni_{1-x}Fe_xO_{3-\delta}$ thin films, Nanoscale, 15 (2023) 1119-1127, http://dx.doi.org/10.1039/D2NR05373J
- [27] L. Wang, P. Adiga, J. Zhao, W.S. Samarakoon, K.A. Stoerzinger, S.R. Spurgeon, B.E. Matthews, M.E. Bowden, P.V. Sushko, T.C. Kaspar, G.E. Sterbinsky, S.M. Heald, H. Wang, L.W. Wangoh, J. Wu, E.-J. Guo, H. Qian, J. Wang, T. Varga, S. Thevuthasan, Z. Feng, W. Yang, Y. Du, S.A. Chambers, Understanding the Electronic Structure Evolution of Epitaxial LaNi_{1-x}Fe_xO₃ Thin Films for Water Oxidation, Nano Lett., 21 (2021) 8324-8331, https://doi.org/10.1021/acs.nanolett.1c02901
- [28] D. Friebel, M.W. Louie, M. Bajdich, K.E. Sanwald, Y. Cai, A.M. Wise, M.-J. Cheng, D. Sokaras, T.-C. Weng, R. Alonso-Mori, R.C. Davis, J.R. Bargar, J.K. Nørskov, A. Nilsson, A.T. Bell, Identification of Highly Active Fe Sites in (Ni,Fe)OOH for Electrocatalytic Water Splitting, J. Am. Chem. Soc., 137 (2015) 1305-1313, https://doi.org/10.1021/ja511559d
- [29] R.P. Forslund, W.G. Hardin, X. Rong, A.M. Abakumov, D. Filimonov, C.T. Alexander, J.T. Mefford, H. Iyer, A.M. Kolpak, K.P. Johnston, K.J. Stevenson, Exceptional electrocatalytic oxygen evolution via tunable charge transfer interactions in La_{0.5}Sr_{1.5}Ni_{1-x}Fe_xO_{4±δ} Ruddlesden-Popper oxides, Nat. Commun., 9 (2018) 3150, https://doi.org/10.1038/s41467-018-05600-y
- [30] M.S. Burke, S. Zou, L.J. Enman, J.E. Kellon, C.A. Gabor, E. Pledger, S.W. Boettcher, Revised Oxygen Evolution Reaction Activity Trends for First-Row Transition-Metal (Oxy)hydroxides in Alkaline Media, J. Phys. Chem. Lett., 6 (2015) 3737-3742, https://doi.org/10.1021/acs.jpclett.5b01650
- [31] L. Trotochaud, S.L. Young, J.K. Ranney, S.W. Boettcher, Nickel-iron oxyhydroxide oxygenevolution electrocatalysts: The role of intentional and incidental iron incorporation, 136 (2014) 6744-6753, https://pubs.acs.org/doi/pdf/10.1021/ja502379c
- [32] L. Liu, L.P. Twight, J.L. Fehrs, Y. Ou, D. Sun, S.W. Boettcher, Purification of Residual Ni and Co Hydroxides from Fe-Free Alkaline Electrolyte for Electrocatalysis Studies, ChemElectroChem, 9 (2022) e202200279, https://doi.org/10.1002/celc.202200279
- [33] T. Binninger, R. Mohamed, K. Waltar, E. Fabbri, P. Levecque, R. Kötz, T.J. Schmidt, Thermodynamic explanation of the universal correlation between oxygen evolution activity and corrosion of oxide catalysts, Scientific Reports, 5 (2015) 12167, https://doi.org/10.1038/srep12167
- [34] C.J. Kaminsky, S. Weng, J. Wright, Y. Surendranath, Adsorbed cobalt porphyrins act like metal surfaces in electrocatalysis, Nat. Catal., 5 (2022) 430-442, https://doi.org/10.1038/s41929-022-00791-6 [35] D.A. Corrigan, The Catalysis of the Oxygen Evolution Reaction by Iron Impurities in Thin Film Nickel Oxide Electrodes, J. Electrochem. Soc., 134 (1987) 377-384, http://dx.doi.org/10.1149/1.2100463 [36] L. Trotochaud, J.K. Ranney, K.N. Williams, S.W. Boettcher, Solution-Cast Metal Oxide Thin Film
- Electrocatalysts for Oxygen Evolution, J. Am. Chem. Soc., 134 (2012) 17253-17261, https://doi.org/10.1021/ja307507a
- [37] L. Trotochaud, S.L. Young, J.K. Ranney, S.W. Boettcher, Nickel–Iron Oxyhydroxide Oxygen-Evolution Electrocatalysts: The Role of Intentional and Incidental Iron Incorporation, J. Am. Chem. Soc., 136 (2014) 6744-6753, https://doi.org/10.1021/ja502379c
- [38] J.R. Petrie, V.R. Cooper, J.W. Freeland, T.L. Meyer, Z. Zhang, D.A. Lutterman, H.N. Lee, Enhanced Bifunctional Oxygen Catalysis in Strained LaNiO₃ Perovskites, J. Am. Chem. Soc., 138 (2016) 2488-2491, https://doi.org/10.1021/jacs.5b11713
- [39] Y. Ou, L.P. Twight, B. Samanta, L. Liu, S. Biswas, J.L. Fehrs, N.A. Sagui, J. Villalobos, J. Morales-Santelices, D. Antipin, M. Risch, M.C. Toroker, S.W. Boettcher, Cooperative Fe sites on transition metal (oxy)hydroxides drive high oxygen evolution activity in base, Nat. Commun., 14 (2023) 7688, https://doi.org/10.1038/s41467-023-43305-z
- [40] D.A. Corrigan, R.M. Bendert, Effect of Coprecipitated Metal Ions on the Electrochemistry of Nickel Hydroxide Thin Films: Cyclic Voltammetry in 1M KOH, J. Electrochem. Soc., 136 (1989) 723, https://dx.doi.org/10.1149/1.2096717

- [41] L.J. Enman, M.S. Burke, A.S. Batchellor, S.W. Boettcher, Effects of Intentionally Incorporated Metal Cations on the Oxygen Evolution Electrocatalytic Activity of Nickel (Oxy)hydroxide in Alkaline Media, ACS Catal., 6 (2016) 2416-2423, https://doi.org/10.1021/acscatal.5b02924
- [42] M.L. Weber, G. Lole, A. Kormanyos, A. Schwiers, L. Heymann, F.D. Speck, T. Meyer, R. Dittmann, S. Cherevko, C. Jooss, C. Baeumer, F. Gunkel, Atomistic Insights into Activation and Degradation of La_{0.6}Sr_{0.4}CoO_{3-δ} Electrocatalysts under Oxygen Evolution Conditions, J. Am. Chem. Soc., 144 (2022) 17966-17979, https://doi.org/10.1021/jacs.2c07226
- [43] A.S. Batchellor, S.W. Boettcher, Pulse-electrodeposited Ni-Fe (oxy)hydroxide oxygen evolution electrocatalysts with high geometric and intrinsic activities at large mass loadings, ACS Catal., 5 (2015) 6680-6689, https://pubs.acs.org/doi/abs/10.1021/acscatal.5b01551?src=recsys
- [44] X. Ma, B. Wang, E. Xhafa, K. Sun, E. Nikolla, Synthesis of shape-controlled La₂NiO_{4+δ} nanostructures and their anisotropic properties for oxygen diffusion, Chem. Commun., 51 (2015) 137-140, http://dx.doi.org/10.1039/C4CC07364A
- [45] X.-K. Gu, J.S.A. Carneiro, S. Samira, A. Das, N.M. Ariyasingha, E. Nikolla, Efficient Oxygen Electrocatalysis by Nanostructured Mixed-Metal Oxides, J. Am. Chem. Soc., 140 (2018) 8128-8137, https://doi.org/10.1021/jacs.7b11138
- [46] X. Ma, J.S.A. Carneiro, X.-K. Gu, H. Qin, H. Xin, K. Sun, E. Nikolla, Engineering Complex, Layered Metal Oxides: High-Performance Nickelate Oxide Nanostructures for Oxygen Exchange and Reduction, ACS Catal., 5 (2015) 4013-4019, https://doi.org/10.1021/acscatal.5b00756
- [47] T. Binninger, Thermodynamic explanation of the universal correlation between oxygen evolution activity and corrosion of oxide catalysts., Nat. Sci. Rep., (2015), https://www.nature.com/articles/srep12167.pdf
- [48] S. Bhavaraju, J.F. DiCarlo, D.P. Scarfe, A.J. Jacobson, D.J. Buttrey, Electrochemical oxygen intercalation in La₂NiO_{4+δ} crystals, Solid State Ion., 86-88 (1996) 825-831, https://www.sciencedirect.com/science/article/pii/0167273896001919
- [49] M.B. Stevens, C.D.M. Trang, L.J. Enman, J. Deng, S.W. Boettcher, Reactive Fe-Sites in Ni/Fe (Oxy)hydroxide Are Responsible for Exceptional Oxygen Electrocatalysis Activity, J. Am. Chem. Soc., 139 (2017) 11361-11364, https://doi.org/10.1021/jacs.7b07117
- [50] R.M. Cornell, U. Schwertmann, The Iron Oxides: Structure, Properties, Reactions, Occurrences, and Uses, 2nd Edition, Wiley-VCH, 2003.
- [51] R.A. Márquez, K. Kawashima, Y.J. Son, G. Castelino, N. Miller, L.A. Smith, C.E. Chukwuneke, C.B. Mullins, Getting the Basics Right: Preparing Alkaline Electrolytes for Electrochemical Applications, ACS Energy Lett., 8 (2023) 1141-1146, https://doi.org/10.1021/acsenergylett.2c02847
- [52] L. Wang, K.A. Stoerzinger, L. Chang, X. Yin, Y. Li, C.S. Tang, E. Jia, M.E. Bowden, Z. Yang, A. Abdelsamie, L. You, R. Guo, J. Chen, A. Rusydi, J. Wang, S.A. Chambers, Y. Du, Strain Effect on Oxygen Evolution Reaction Activity of Epitaxial NdNiO₃ Thin Films, ACS Appl. Mater. Interfaces, 11 (2019) 12941-12947, https://doi.org/10.1021/acsami.8b21301
- [53] W.T. Hong, K.A. Stoerzinger, Y.-L. Lee, L. Giordano, A. Grimaud, A.M. Johnson, J. Hwang, E.J. Crumlin, W. Yang, Y. Shao-Horn, Charge-transfer-energy-dependent oxygen evolution reaction mechanisms for perovskite oxides, Energy Environ. Sci., 10 (2017) 2190-2200, http://dx.doi.org/10.1039/C7EE02052J
- [54] J. Suntivich, H.A. Gasteiger, N. Yabuuchi, H. Nakanishi, J.B. Goodenough, Y. Shao-Horn, Design principles for oxygen-reduction activity on perovskite oxide catalysts for fuel cells and metal–air batteries, Nat. Chem., 3 (2011) 546-550, https://doi.org/10.1038/nchem.1069
- [55] Y. Sun, J. Wang, S. Xi, J. Shen, S. Luo, J. Ge, S. Sun, Y. Chen, J.V. Hanna, S. Li, X. Wang, Z.J. Xu, Navigating surface reconstruction of spinel oxides for electrochemical water oxidation, Nat. Commun., 14 (2023) 2467, https://doi.org/10.1038/s41467-023-38017-3
- [56] A. Grimaud, O. Diaz-Morales, B. Han, W.T. Hong, Y.-L. Lee, L. Giordano, K.A. Stoerzinger, M.T.M. Koper, Y. Shao-Horn, Activating lattice oxygen redox reactions in metal oxides to catalyse oxygen evolution, Nat. Chem., 9 (2017) 457-465, https://doi.org/10.1038/nchem.2695

- [57] S. Samira, X.-K. Gu, E. Nikolla, Design Strategies for Efficient Nonstoichiometric Mixed Metal Oxide Electrocatalysts: Correlating Measurable Oxide Properties to Electrocatalytic Performance, ACS Catal., 9 (2019) 10575-10586, https://doi.org/10.1021/acscatal.9b02505
- [58] J.R. Rumble, J.C.H.o.C.a.P. Rumble, 98th Edition, C.H.o.C.a. Physics, CRC Press LLC, CRC Handbook of Chemistry and Physics, 103rd Edition, CRC Press LLC, 2021.
- [59] W. Zhou, H.F. Greer, What Can Electron Microscopy Tell Us Beyond Crystal Structures?, Eur. J. Inorg. Chem., 2016 (2016) 941-950, <a href="https://chemistry-public.com/https://chemistry-
- europe.onlinelibrary.wiley.com/doi/abs/10.1002/ejic.201501342
- [60] C. Dette, M.R. Hurst, J. Deng, M.R. Nellist, S.W. Boettcher, Structural Evolution of Metal (Oxy)hydroxide Nanosheets during the Oxygen Evolution Reaction, ACS Appl. Mater. Interfaces, 11 (2019) 5590-5594, https://doi.org/10.1021/acsami.8b02796
- [61] J. Deng, M.R.N. Nellist, M.B. Stevens, C. Dette, Y. Wang, S.W. Boettcher, Morphology dynamics of single-layered Ni(OH)₂/NiOOH nanosheets and subsequent Fe incorporation studied by *in situ* electrochemical atomic force microscopy., Nanoletters, 17 (2017) 6922-6926, https://pubs.acs.org/doi/pdf/10.1021/acs.nanolett.7b03313
- [62] M.F. Sunding, K. Hadidi, S. Diplas, O.M. Løvvik, T.E. Norby, A.E. Gunnæs, XPS characterisation of in situ treated lanthanum oxide and hydroxide using tailored charge referencing and peak fitting procedures, J. Electron Spectrosc. Relat. Phenom., 184 (2011) 399-409, https://www.sciencedirect.com/science/article/pii/S0368204811000727
- [63] M.C. Biesinger, B.P. Payne, A.P. Grosvenor, L.W.M. Lau, A.R. Gerson, R.S.C. Smart, Resolving surface chemical states in XPS analysis of first row transition metals, oxides and hydroxides: Cr, Mn, Fe, Co and Ni, Appl. Surf. Sci., 257 (2011) 2717-2730, https://www.sciencedirect.com/science/article/pii/S0169433210014170
- [64] J. San Choi, C.W. Ahn, J.-S. Bae, T.H. Kim, Identifying a perovskite phase in rare-earth nickelates using X-ray photoelectron spectroscopy, Curr. Appl. Phys., 20 (2020) 102-105, https://www.sciencedirect.com/science/article/pii/S1567173919302640
- [65] B.P. Payne, M.C. Biesinger, N.S. McIntyre, Use of oxygen/nickel ratios in the XPS characterisation of oxide phases on nickel metal and nickel alloy surfaces, J. Electron Spectrosc. Relat. Phenom., 185 (2012) 159-166, https://www.sciencedirect.com/science/article/pii/S0368204812000631
- [66] M.C. Biesinger, B.P. Payne, L.W.M. Lau, A. Gerson, R.S.C. Smart, X-ray photoelectron spectroscopic chemical state quantification of mixed nickel metal, oxide and hydroxide systems, Surf. Interface Anal., 41 (2009) 324-332, https://doi.org/10.1002/sia.3026
- [67] R.A. Krivina, G.A. Lindquist, M.C. Yang, A.K. Cook, C.H. Hendon, A.R. Motz, C. Capuano, K.E. Ayers, J.E. Hutchison, S.W. Boettcher, Three-Electrode Study of Electrochemical Ionomer Degradation Relevant to Anion-Exchange-Membrane Water Electrolyzers, ACS Appl. Mater. Interfaces, 14 (2022) 18261-18274, https://doi.org/10.1021/acsami.1c22472
- [68] D.Y. Chung, P.P. Lopes, P. Farinazzo Bergamo Dias Martins, H. He, T. Kawaguchi, P. Zapol, H. You, D. Tripkovic, D. Strmcnik, Y. Zhu, S. Seifert, S. Lee, V.R. Stamenkovic, N.M. Markovic, Dynamic stability of active sites in hydr(oxy)oxides for the oxygen evolution reaction, Nat. Energy, 5 (2020) 222-230, https://doi.org/10.1038/s41560-020-0576-y
- [69] Y.J. Son, S. Kim, V. Leung, K. Kawashima, J. Noh, K. Kim, R.A. Marquez, O.A. Carrasco-Jaim, L.A. Smith, H. Celio, D.J. Milliron, B.A. Korgel, C.B. Mullins, Effects of Electrochemical Conditioning on Nickel-Based Oxygen Evolution Electrocatalysts, ACS Catal., 12 (2022) 10384-10399, https://doi.org/10.1021/acscatal.2c01001
- [70] B.R. Wygant, K. Kawashima, C.B. Mullins, Catalyst or Precatalyst? The Effect of Oxidation on Transition Metal Carbide, Pnictide, and Chalcogenide Oxygen Evolution Catalysts, ACS Energy Lett., 3 (2018) 2956-2966,
- [71] L. Gong, X.Y.E. Chng, Y. Du, S. Xi, B.S. Yeo, Enhanced Catalysis of the Electrochemical Oxygen Evolution Reaction by Iron(III) Ions Adsorbed on Amorphous Cobalt Oxide, ACS Catal., 8 (2018) 807-814, https://doi.org/10.1021/acscatal.7b03509

- [72] S. Yagi, I. Yamada, H. Tsukasaki, A. Seno, M. Murakami, H. Fujii, H. Chen, N. Umezawa, H. Abe, N. Nishiyama, S. Mori, Covalency-reinforced oxygen evolution reaction catalyst, Nat. Commun., 6 (2015) 8249, https://doi.org/10.1038/ncomms9249
- [73] K.J. May, C.E. Carlton, K.A. Stoerzinger, M. Risch, J. Suntivich, Y.-L. Lee, A. Grimaud, Y. Shao-Horn, Influence of Oxygen Evolution during Water Oxidation on the Surface of Perovskite Oxide Catalysts, J. Phys. Chem. Lett., 3 (2012) 3264-3270, https://doi.org/10.1021/jz301414z
- [74] M. Risch, A. Grimaud, K.J. May, K.A. Stoerzinger, T.J. Chen, A.N. Mansour, Y. Shao-Horn, Structural Changes of Cobalt-Based Perovskites upon Water Oxidation Investigated by EXAFS, J. Phys. Chem. C, 117 (2013) 8628-8635, https://doi.org/10.1021/jp3126768
- [75] A. Grimaud, K.J. May, C.E. Carlton, Y.-L. Lee, M. Risch, W.T. Hong, J. Zhou, Y. Shao-Horn, Double perovskites as a family of highly active catalysts for oxygen evolution in alkaline solution, Nat. Commun., 4 (2013) 2439, https://doi.org/10.1038/ncomms3439
- [76] Z. He, J. Zhang, Z. Gong, H. Lei, D. Zhou, N. Zhang, W. Mai, S. Zhao, Y. Chen, Activating lattice oxygen in NiFe-based (oxy)hydroxide for water electrolysis, Nat. Commun., 13 (2022) 2191, https://doi.org/10.1038/s41467-022-29875-4
- [77] I.C. Man, H.-Y. Su, F. Calle-Vallejo, H.A. Hansen, J.I. Martínez, N.G. Inoglu, J. Kitchin, T.F. Jaramillo, J.K. Nørskov, J. Rossmeisl, Universality in Oxygen Evolution Electrocatalysis on Oxide Surfaces, ChemCatChem, 3 (2011) 1159-1165, https://doi.org/10.1002/cctc.201000397
- [78] J.S.A. Carneiro, J. Williams, A. Gryko, L.P. Herrera, E. Nikolla, Embracing the Complexity of Catalytic Structures: A Viewpoint on the Synthesis of Nonstoichiometric Mixed Metal Oxides for Catalysis, ACS Catal., 10 (2020) 516-527, https://doi.org/10.1021/acscatal.9b04226
- [79] M.B. Stevens, L.J. Enman, A.S. Batchellor, M.R. Cosby, A.E. Vise, C.D.M. Trang, S.W. Boettcher, Measurement Techniques for the Study of Thin Film Heterogeneous Water Oxidation Electrocatalysts, Chemistry of Materials, 29 (2017) 120-140, https://doi.org/10.1021/acs.chemmater.6b02796